International Journal of Mechanical Sciences 160 (2019) 209–218

Contents lists available at ScienceDirect

International Journal of Mechanical Sciences

journal homepage: www.elsevier.com/locate/ijmecsci

Influence of arterial mechanical properties on carotid blood flow: Comparison of CFD and FSI studies

D. Lopes[a], H. Puga[a,*], J.C. Teixeira[b], S.F. Teixeira[c]

[a] CMEMS-UMinho, Department of Mechanical Engineering School of Engineering, University of Minho, Campus of Azurém, 4800-058 Guimarães, Portugal
[b] MEtriCS, Department of Mechanical Engineering School of Engineering, University of Minho, Campus of Azurém, 4800-058 Guimarães, Portugal
[c] Algoritmi, Department of Production and Systems School of Engineering, University of Minho, Campus of Azurém, 4800-058 Guimarães, Portugal

ARTICLE INFO

Keywords:
Atherosclerosis
Blood flow
Carotid artery bifurcation
Fluid-structure interaction

ABSTRACT

Carotid artery blood flow is studied to compare models with rigid and elastic walls. Considering a patient-specific geometry and transient boundary conditions. In the case of rigid walls, only the fluid (blood) behavior is considered, in a typical Computational Fluid Dynamics study. With the elastic walls, the reciprocal influence of both fluid and solid (blood and artery) are taken into account, constituting a Fluid-Structure Interaction study. Furthermore, the study of the influence of mechanical properties of the artery, which become stiffer with the progression of atherosclerosis, on blood flow is also presented, an innovative approach relative to the work done in this field. Results show that the carotid sinus is the preferential zone to develop atherosclerosis, given its low values of Time-Averaged Wall Shear Stress. Additionally, it is fundamental to consider the arterial wall as elastic bodies, given that the rigid model overestimates the flow velocity and Wall Shear Stress. On the different mechanical properties of the vessel, its influence is minimal in the Time-Averaged Wall Shear Stress profiles. However, given the results of the displacement and velocity profiles, their inclusion in blood flow simulations in stenosed arteries should be considered.

1. Introduction

Atherosclerosis is a precursory pathology of cardiovascular diseases, such as stroke and heart attacks, which are the main causes of death in developed countries [1,2]. Such pathology is characterized by the accumulation of fat particles, cholesterol, and other substances on the walls of large and medium-sized arteries. At an early stage, atherosclerosis does not present significant symptoms, however, with its evolution, there is a substantial reduction of the lumen of the artery, called stenosis, which in very advanced phases can compromise the blood supply to the organs downstream of it, thus causing the ischemic problems. On the other hand, this disease is associated with an increase of arterial stiffness [3–5], which under certain conditions can cause plaque rupture and trigger thrombosis inside the arteries [6]. Furthermore, Atherosclerosis is a geometrically focal disease prone to involve the outer edges of blood vessel bifurcations, as is the case of the carotid artery bifurcation, where the highest incidence of this disease occurs [7]. Each individual has two carotid arteries, which are located in the anterior region of the neck and are responsible for transporting oxygenated blood from the heart to the brain, thus being the origin of most cerebral vascular problems. According to several authors [8–12], local hemodynamic factors are important determinants of atherosclerotic plaque development and progression.

The study of blood flow is thus important in understanding the mechanisms behind the onset and progression of Atherosclerosis. Several methods have been used for the in vivo study of flow-related variables, such as the use of magnetic resonance imaging (MRI) [13–15], Doppler ultrasonography [15–18], particle-based methods such as: streak photography, particle tracking velocimetry (PTV), particle image velocimetry (PIV), and micro-particle image velocimetry (μPIV) [19]. These techniques require the use of specific equipment and are, therefore, associated with high investment and operating costs. Moreover, it is necessary to have good infrastructures and patients available for the in vivo studies, which the whole process makes difficult. Thereby, numerical simulation emerges as a cheaper and more efficient alternative to predict the behavior of blood. Simulation methods also provide the chance to study atherosclerosis specifically for each patient and to design customized stents for that particular individual, thus providing a better treatment to the patient. Regarding the validity of the simulations, Long et al. [20] stated that there is a high correlation between MRI velocity measurements and numerical predictions shown in the computational fluid dynamics (CFD) study. Additionally, Cibis et al. [21] studied the blood flow in the carotid artery through MRI and a CFD study and obtained similar results with both methods, thus it is emphasized that numerical simulation methods are able to yield robust and reliable results.

More recently, CFD techniques have been extensively used in the study of the hemodynamics of the carotid artery bifurcation [8,22,23],

* Corresponding author.
E-mail address: puga@dem.uminho.pt (H. Puga).

https://doi.org/10.1016/j.ijmecsci.2019.06.029
Received 23 January 2019; Received in revised form 4 June 2019; Accepted 17 June 2019
Available online 18 June 2019

given the high incidence of stenosis in this vessel and the fact that its superficial location makes it less challenging to image than other arterial bifurcations. In these, there is only considered one domain, the fluid domain, and the behavior of the artery is approximated to that of a rigid body, which is a limitation since the artery has a direct impact in blood behavior. Two-way fluid-structure interaction (FSI) couples CFD simulations with finite element analysis (FEA) of the vessel wall. This multiphysics coupling considers the influence of blood on the artery and vice-versa, therefore, is a more realistic approach to simulating the process. However, FSI requires additional modeling assumptions regarding the mechanical properties of the vessel and significantly more computational effort. With the development of computational power in the last decade, researchers have applied fluid-structure interaction the study of blood flow in healthy and stenosed vessels [24–26]. Although many advances are reported, the change in the mechanical properties of the arterial walls with the progression of Atherosclerosis is commonly ignored. Such evidence is related to the difficult to experimentally measure the impact of the disease on the elasticity of the vessels, being this the main gap of the current research done in this field.

In this work, the numerical simulations of fluid and solid mechanics in an anatomically realistic carotid artery bifurcation model are presented. In the first place, the comparison between a typical CFD study, where the wall is considered rigid, and a two-way fully coupled transient FSI problem, where the wall is flexible, is shown. The hemodynamic parameters, such as the velocity, pressure, wall shear stress are compared to assess the extent to which it is worth to do the FSI studies since the simulations are much more demanding in the latter. It is also sought to make the association between local hemodynamics and the areas conducive to develop atherosclerosis. In another scope, the study of the influence of arterial stiffness is presented, which increases with the progression of the disease in question and age [27]. In this, four models of arterial material with a different elastic modulus were used in order to evaluate the influence of the parameter in the results.

2. Methods

2.1. Blood flow modeling

Blood flow in the carotid artery was assumed to be incompressible, laminar, Newtonian. Therefore, the governing equations used to describe the flow are the continuity equation, Eq. (1), and Navier-Stokes equations, Eq. (2).

$$\rho_f \nabla . \vec{V} = 0 \tag{1}$$

$$\frac{\partial \vec{V}}{\partial t} + \rho_f \left(\vec{V}.\nabla\right) \vec{V} = - \nabla p + \nabla \overline{\overline{\tau}} \tag{2}$$

where t represents time, ρ_f is the fluid density, $\vec{V}$, the velocity vector, p, the fluid pressure and $\overline{\overline{\tau}}$, the viscous stress tensor. Eq. (1) states that the local increase of density with time is balanced by a divergence of a mass flux. Eq. (2) states that the rate of change of momentum in a fluid particle is equal to the sum of the forces in it. The forces in a fluid particle assumed in this work are pressure and viscous forces, which are represented in the second term of Eq. (2). Body forces such as gravity have been neglected.

It is common to approximate the behavior of blood to a Newtonian fluid [8,22]. This assumption can be explained by the fact that the vessel diameters are large compared to the individual red blood cell diameters [28–30], which makes the blood viscosity independent of the shear rate and therefore constant.

2.2. Modeling arterial deformation

According to Newton's second law of motion, the total linear momentum is equal to the sum of the external forces working on a volume.

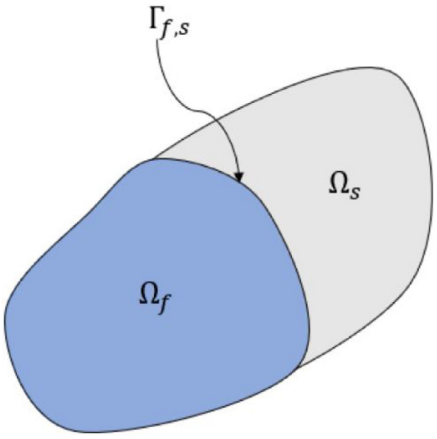

Fig. 1. FSI domains and boundary interface.

The linear momentum conservation principle is the base of the governing equation for the vessel wall deformation, Eq. (3).

$$\rho_s \frac{\partial^2 u}{\partial t^2} - \nabla \overline{\overline{\sigma}} = \rho_s \vec{b} \tag{3}$$

where ρ_s is the density of the solid, u represents the displacements of the solid, $\vec{b}$, the body forces applied on the structure, $\overline{\overline{\sigma}}$, the Cauchy stress tensor. For an isotropic linear elastic solid, the stress tensor becomes [31]:

$$\overline{\overline{\sigma}} = 2 \mu_L \overline{\overline{\varepsilon}} + \lambda_L \, tr\left(\overline{\overline{\varepsilon}}\right) I \tag{4}$$

where λ_L and μ_L are the first and second Lamé parameters, respectively, ε, the strain tensor, tr, the trace function, and I, the identity matrix. For compressible materials, Lamé parameters can be written as a function of the elastic modulus, E, and Poisson's coefficient, v.

$$\lambda_L = \frac{v\, E}{(1+v)(2v-1)} \tag{5}$$

$$\mu_L = \frac{E}{2\,(1+v)} \tag{6}$$

2.3. Modeling fluid-structure interaction

In FSI problems, neither the Lagrangian nor the Eulerian formulations are optimal for the entire domain. The first cannot handle the large deformations of the fluid, and a Eulerian formulation sacrifices some accuracy when applied to solids [32]. The Arbitrary Lagrangian-Eulerian (ALE) method is used for FSI problems, where the grid of the fluid domain is allowed to deform arbitrarily so that its boundaries follow the structural domains' deformation. The structural problem is then formulated in the Lagrangian way, combining the two approaches.

With the ALE method, it is not enough to have the governing equations of the flow and the vessel wall deformation, it is also necessary to mathematically describe the coupling of the two domains, which involves governing equations for the fluid-solid interface.

Fig. 1 shows a regular FSI problem with a fluid domain Ω_f and a solid domain Ω_s, which are independent from each other and interact along with common the shared interface, $\Gamma_{f,s}$.

The FSI problem requires that there are mass conservation and conservation of linear momentum along with the interface [31]. These principles are satisfied by the displacement compatibility and traction equilibrium at $\Gamma_{f,s}$, accordingly to Eqs. (7) and (8).

$$u_{f,\Gamma} = u_{s,\Gamma} \tag{7}$$

$$\overrightarrow{t_{f,\Gamma}} = \overrightarrow{t_{s,\Gamma}} \tag{8}$$

where $u_{f,\Gamma}$ is the displacement of the fluid at the interface, $u_{s,\Gamma}$, the displacement of the solid at the interface, $\overrightarrow{t_{f,\Gamma}}$, the forces of the fluid on the

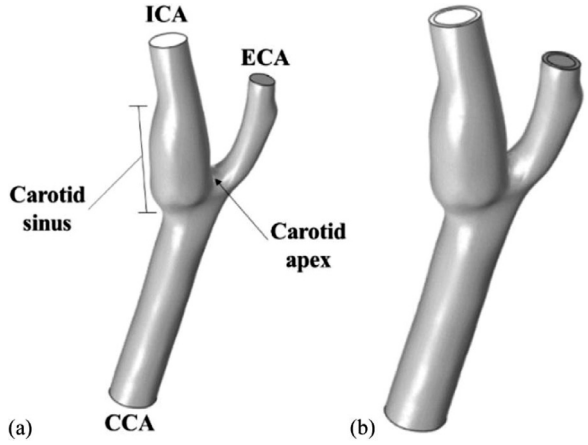

Fig. 2. Geometry of the carotid artery bifurcation. (a) CFD study; (b) FSI study.

Table 1
Dimensions of the inlet and outlet sections.

Section	Area (mm^2)	Diameter (mm)
CCA	30.898	6.272
ICA	14.670	4.322
ECA	7.184	3.024

interface and $\overrightarrow{t_{s,\Gamma}}$, the forces of the solid on interface. Eq. (8) is often written as.

$$\overline{\overline{\sigma_s}} \cdot \overrightarrow{n_{s,\Gamma}} = p_{f,\Gamma}.\overrightarrow{n_{f,\Gamma}} - \overline{\overline{\tau_{f,\Gamma}}}.\overrightarrow{n_{f,\Gamma}} \quad (9)$$

where $\overline{\overline{\sigma_s}}$ is the stress tensor, $\overrightarrow{n_{s,\Gamma}}$ and $\overrightarrow{n_{f,\Gamma}}$ are the solid and fluid interface normals, $p_{f,\Gamma}$, the interface pressure and $\overline{\overline{\tau_{f,\Gamma}}}$ the viscous stress tensor.

2.4. Material properties

Blood was modeled as a Newtonian fluid, with a density $\rho_f = 1,060$ kg/m^3 and dynamic viscosity, $\mu = 3.5 \times 10^{-3}$ Pa .s [8]. Regarding the mechanical properties of the vessel, the artery was modelled as a linear elastic isotropic material with a density $\rho_s = 1,120$ kg/m^3, Poisson's ratio, $\nu = 0.45$, and elastic modulus, $E = 1.106 \times 10^6$ Pa [33]. In order to study the influence of the arterial stiffness on blood flow, three FSI simulations were performed with different values of the elastic modulus, which correspond to an increase of 20% (FSI 1.2 E, $E = 1.270 \times 10^6$ Pa), 50% (FSI 1.5 E, $E = 1.590 \times 10^6$ Pa), and 100% (FSI 2.0 E, $E = 2.12 \times 10^6$ Pa), relatively to the original value.

2.5. Geometry, mesh and domain considerations

The geometry of the carotid artery bifurcation, which is shown in Fig. 2(a), was used for the CFD study [34]. Since it only corresponds to the fluid domain, obviously, it is not applicable to the FSI studies. The arterial domain, which is also represented in Fig. 2(b), was subsequently built with CAD software, with several offsets of the fluid domain surfaces depicted in Fig. 2(a). A thickness of 1 mm was considered for the carotid artery, according to [33].

Regarding the nomenclature of the geometry, upstream the bifurcation is the common carotid artery, hereinafter referred to as CCA, which represents the inlet. Downstream the bifurcation are the internal carotid artery (ICA) and external carotid artery (ECA), which represent the outlets. The dilation that exists in the ICA is called carotid sinus, or carotid bulb, and the zone of separation between the two outlet arteries is named carotid apex. Table 1 shows the areas of the sections of the mentioned boundaries.

The fluid domain was discretized in 867,348 tetrahedral elements and the solid domain in 145,635 elements of the same type, thus forming a tetrahedral mesh of 1012,983 in total for the FSI studies. A mesh convergence study was done to ensure that the results are independent of the mesh. In Fig. 3 is represented a summary of the convergence study and represents the velocity magnitude taken from a point within the fluid domain, at the systolic peak, for four different mesh sizes.

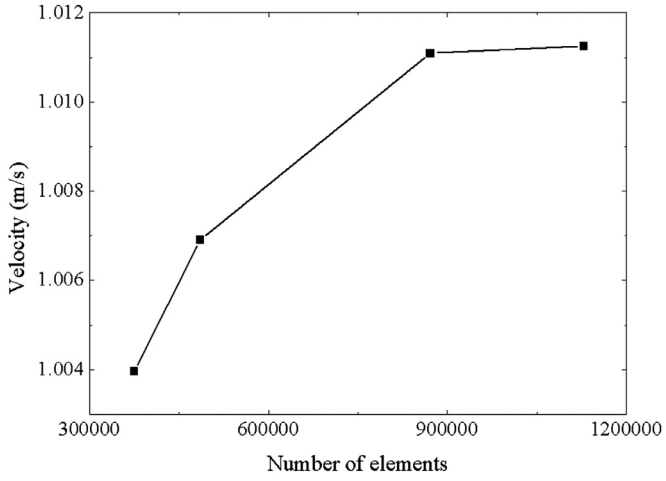

Fig. 3. Variation of the velocity magnitude with mesh refinement.

The results show that an increase from 867,348 to 1,128,970 in the fluid mesh elements only presents an effect of 0.015% in the velocity magnitude. Furthermore, the increase of mesh elements (23%) took approximately 220% more time to simulate the model, and the differences in the velocity results suggest be negligible.

The governing equations were solved with COMSOL Multiphysics simulation software, version 5.2 a. The transient CFD study was carried out with GMRES, an iterative solver, with the iterations limited to a maximum number of 25. In this case, the convergence was accepted when the residuals were below 10^{-5}. The transient two-way FSI study was carried out with PARDISO, a direct solver that is based on lower-upper decomposition. The iterations were limited to a maximum number of 25, with the same residual's tolerance. A free time-step was used in every simulation, which means that the solver takes smaller or larger time-steps to satisfy the required tolerances.

Every study was performed over three full cardiac cycles to minimize the effect of the initial conditions, which generate instability in the model, and the results were taken from the third cycle. The simulations were performed with an Intel i7-6700 HQ Core of a personal computer, with 16GB of RAM, that runs 64-bit Windows 7.

2.6. Boundary conditions

For the inlet, CCA, it was imposed a volumetric flow rate profile, considering a heart rate of 60 bpm, which means that the cardiac cycle is repeated every 1 s. This evidence reflects the pulsatile nature of the human cardiac cycle, with the two distinct phases, systole and diastole, well defined. The flow rate has a maximum flow rate value for $t = 0.21$ s and represents the systole peak. It was also assumed that the flow is completely developed at the inlet, with a parabolic profile along with it, accordingly to [8,35,36]. For the outlets, ICA and ECA, a pressure waveform was applied for both as a boundary condition. The maximum pressure occurs for $t = 0.45$ s, which means that there is a shift between the instant of maximum flow and maximum pressure during the cardiac cycle. This time delay is due to the compliance of the downstream vasculature [8]. Both flow rate and pressure profiles are represented in Fig. 4. Relatively to the solid model, the adjacent boundaries to the inlet and outlet were fixed. The remaining boundaries of the solid, a condition of free deformation was applied, which basically allows the solid to deform in any direction.

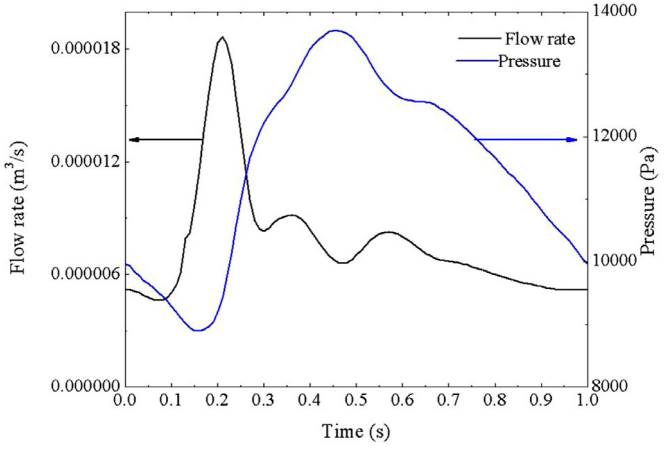

Fig. 4. Flow rate profile imposed at the inlet (CCA); pressure waveform imposed at the outlets (ICA and ECA) [8].

Considering the maximum flow rate imposed at the inlet and the area of the CCA section shown in Table 1, Eq. (10) was used to obtain an average velocity value.

$$Q = V.A \tag{10}$$

where Q is the flow rate (m^3/s), V, the velocity magnitude (m/s) and A, the surface area of the inlet section (mm^2). The average velocity value was used to calculate the Reynolds number, with Eq. (11).

$$Re = \frac{\rho_f V D}{\mu} \tag{11}$$

where ρ_f is the fluid density (kg/m^3), V, the velocity magnitude (m/s), D, the diameter of the artery and μ the dynamic viscosity (Pa .s). The value obtained was 1146, therefore the assumption of a laminar flow was reasonable.

2.7. Hemodynamic parameters

In order to associate the local hemodynamics to Atherosclerosis prone areas, the following hemodynamic parameters were calculated: (i) Wall Shear Stress (WSS) and (ii) Time-Averaged Wall Shear Stress (TAWSS).

WSS is the frictional force per unit area exerted by the circulating blood column on the intimal surface of the arteries. In COMSOL, this parameter is obtained with the vorticity lines on the surface, according to Eq. (12) [37].

$$\overrightarrow{\tau_w} = \mu .\left(\omega_{Wall}.\overrightarrow{n}\right) \tag{12}$$

where μ is dynamic viscosity, ω_{Wall} is vorticity at the wall and $\overrightarrow{n}$ is the outer normal unit vector of the tangential plane to the vessel wall. According to the literature [8–12,18,38,39], atherosclerosis prone regions are subject to low and oscillating WSS values, that is, the values are oscillatory when the WSS vector has a direction contrary to the direction of flow, which means that there is fluid recirculation in these areas.

The Time-Averaged Wall Shear Stress (TAWSS) is a hemodynamic index that represents an average temporal evaluation of the magnitude of the WSS over a cycle, which is calculated for each node, with Eq. (13).

$$TAWSS = \frac{1}{t}\int_0^T \left|\overrightarrow{\tau_w}\right| dt \tag{13}$$

where T, represents the period of the cardiac cycle and $|\overrightarrow{\tau_w}|$ is the modulus of the wall shear stress vector.

According to the literature [38,40], TAWSS magnitude typically ranges from 0.1 to 0.6 Pa in the venous system, from 1 to 7 Pa in normal arteries and from 0 to 0.4 Pa in atherosclerosis-prone arterial regions.

3. Results

3.1. Flow separation

Fig. 5 illustrates the distribution of the flow rate through the outlets, ECA and ICA, during a complete cardiac cycle, for all the cases studied.

According to Fig. 5, the graphs that represent the separation of flow are equivalent for all the studied cases. It is observed that most of the flow leaves the system through the ICA. The ratio between the ECA and ICA mass flow ratio is represented in Fig. 6.

The ECA/ICA ratio plot shows that there is a minor increase in the ratio during the systole phase, being practically constant in the remainder of the cardiac cycle. While the lines of the FSI studies overlap, which indicates that the elasticity of the artery has no impact on fluid separation, there is a slight difference from the CFD and FSI studies results. Table 2 contains statistical data that complements the information given by the graphs of Figs. 5 and 6.

The time-averaged flow rate in the ICA represents about 69% of the inflow rate for every study, which is in accordance with the measurements of [41]. Furthermore, the standard deviation of the flow through the ICA decreases with the increased arterial wall stiffness, being minimum for the CFD study, where the wall has no movement. As a conclusion, it is noted that the maximum flow rate that passes through the ICA is slightly higher for the FSI study, and as the rigidity increases, the values get closer to the CFD model. Although there are some differences in the data of Table 2, these are minimal when the whole cardiac cycle is considered and it can be concluded that the influence of the flexible wall and the several elastic moduli are negligible concerning the separation of the flow through the outlets. Furthermore, it should be noted that the resistance of the downstream vessels is the main factor that influences the separation of the flow through the outlets, with blood flowing preferentially in the vessel of least resistance. However, in this work, the same pressure profile was applied for both ICA and ECA, it is concluded that the minimal differences in the results are due to the changes in the cross-sectional area at the bifurcation, resulting from the elastic effect of the wall.

3.2. Velocity

Fig. 7 represents the velocity profiles for every study, considering the moment of maximum inflow rate, at the systolic peak.

By the results stated in Fig. 7, it is verified that the velocity profile is parabolic, or fully developed, at the inlet, with a maximum value in the middle of the section and a progressive decrease as it approaches the

Table 2
Statistical data relative to the separation of flow through the outlets.

	CFD		FSI		FSI 1.2 E		FSI 1.5 E		FSI 2 E	
	ICA	ECA	ICA	ECA	ICA	ECA	ICA	ECA	ICA	ECA
Time-average flow rate (%)	69.56	30.44	69.91	30.09	69.85	30.15	69.79	30.21	69.70	30.30
Standard deviation (%)	0.85	0.85	2.45	2.45	2.12	2.12	1.79	1.79	1.48	1.48
Maximum difference on flow rate (%)	70.84	29.16	74.36	25.64	72.75	27.25	71.98	28.02	71.55	28.45
Minimum difference on flow rate (%)	67.81	32.19	64.23	35.77	64.75	35.25	65.44	34.56	66.17	33.83

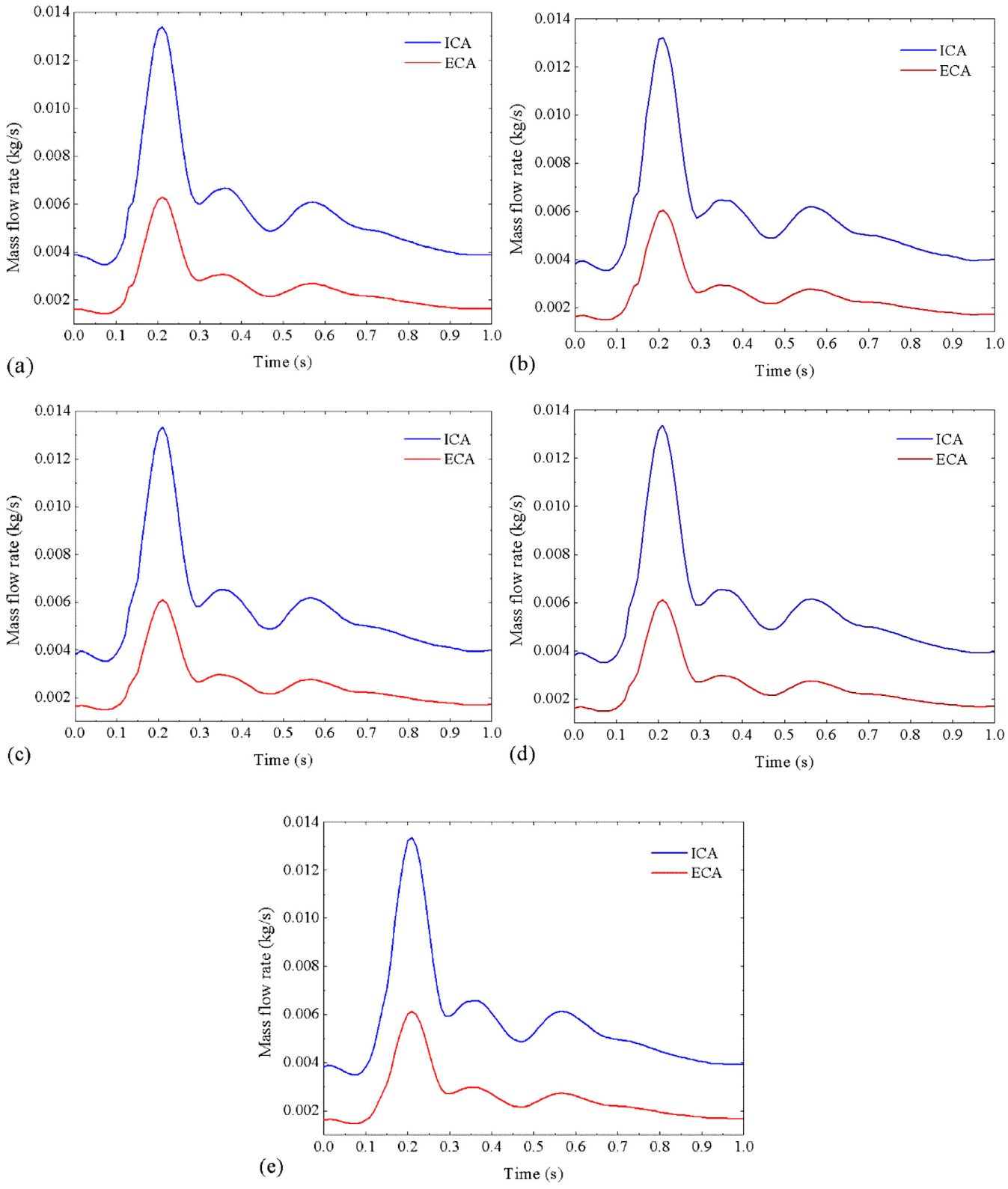

Fig. 5. Distribution of the flow rate to the outlets. (a) rigid model (CFD); elastic models :(b) FSI; (c) FSI 1.2 E; (d) FSI 1.5 E; (e) FSI 2.0 E.

wall, where the velocity is zero. The profile remains so until it encounters the bifurcation, where it is largely distorted, causing most of the fluid to flow close to the inner walls of the outlet arteries, whereas in the outer zones, such as in the carotid sinus, the amount of circulating fluid is substantially less. It is also noted that there is a large difference between the magnitude of the velocity between the CFD and FSI studies, mainly in the CCA and the anterior zones of arteries downstream the bifurcation, which can be justified by the fact that the wall is flexible and expands with the fluid pressure, thus increasing the size of the lumen. With the increase of the cross-section, for a constant flow rate, the veloc-

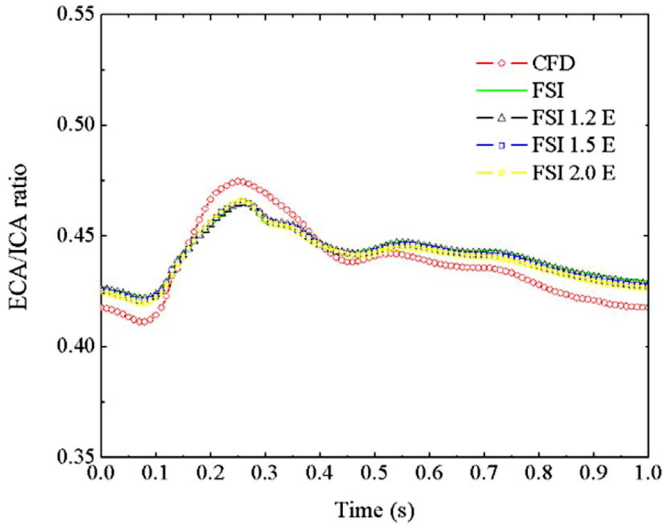

Fig. 6. Ratio between the mass flow rate of the outlet arteries (ECA/ICA).

ity decreases. Near the outlets, the difference in the velocity magnitude results is smaller, which is justified by the elastic effect of the artery, where it, firstly, expands due to the effect of the fluid, and later, when compressing, squeezes the fluid in turn and increases its velocity, thus allowing a more uniform supply of blood to the outlet vessels.

Comparing the results of the various FSI studies, it is observed that there is a small increase in the magnitude of the overall velocity for the models with higher rigidity, which is due to the smaller deformations of the wall induced by the fluid.

Despite the differences observed, the magnitude of the velocity for both CFD and FSI studies is within range with the measurements of [14,16] and the results obtained by [8], which reinforces the validity of the performed simulations. The graphs of Fig. 8 represent the velocity magnitude at three distinct points, which are located in the CCA, ICA, and ECA, respectively.

Relatively the results in the CCA point, the magnitude of the velocity is found to be significantly higher for the CFD study, particularly at the systolic peak and throughout the whole diastolic phase. For the ICA, the results show that the difference between the CFD and FSI is minimal, except for the initial instants of the diastole. In the case of the ECA, the results show similar values of velocity for every phase of the cardiac cycle, between the CFD and FSI studies. In fact, there was no major difference in the magnitude of velocity in the outlet arteries, which is due to the elastic effect of the artery wall that is extremely important for the reason that it guarantees a continuous supply of blood to the tissues, despite the heart works in cycles and interrupts the supply of blood to the aorta.

Comparing the results of the FSI studies, it is noted that there is a slight increase in the magnitude of the velocity in the cases of higher elastic modulus (FSI 2.0) when compared to the normal value (FSI). As arteries become stiffer, that is, as the elastic modulus increases, they are expected to deform less with the pressure of the fluid, which allows the fluid to flow slightly faster. The maximum difference between the

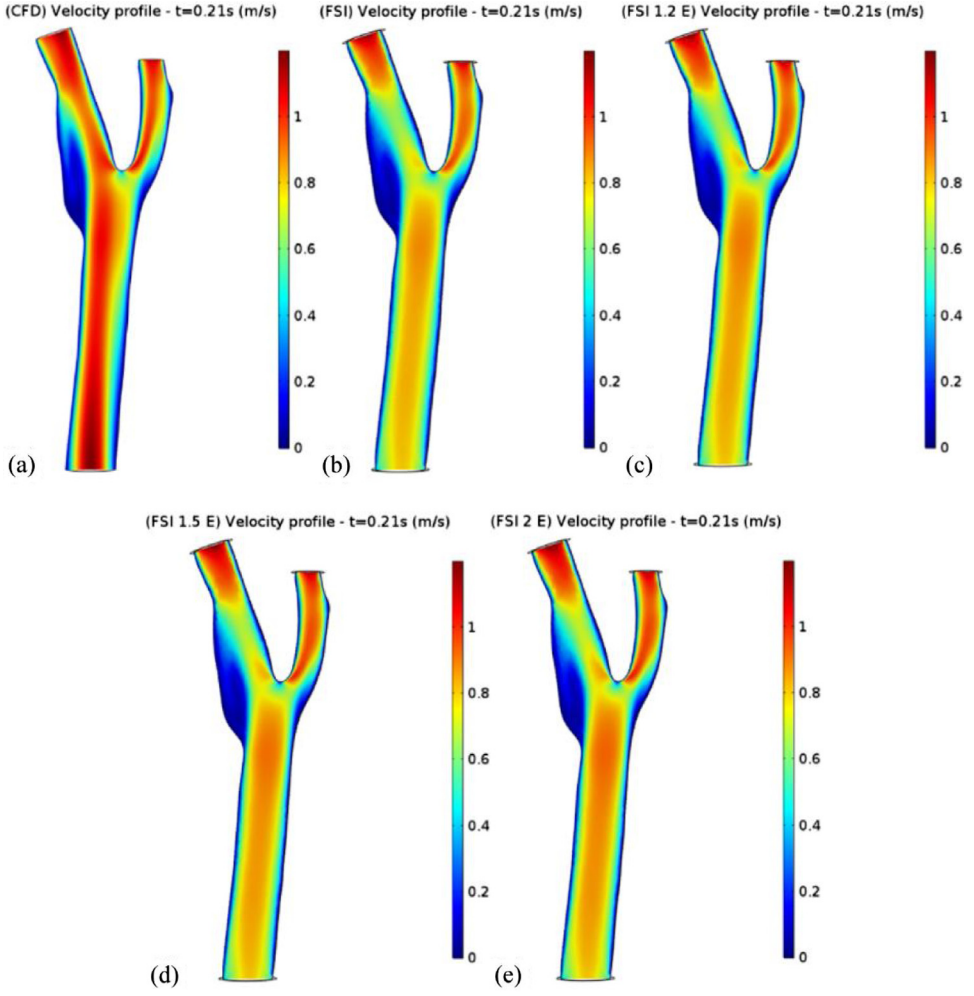

Fig. 7. Velocity profile at systolic peak ($t = 0.21$ s). (a) CFD; (b) FSI; (c) FSI 1.2 E; (d) FSI 1.5 E; (e) FSI 2.0 E.

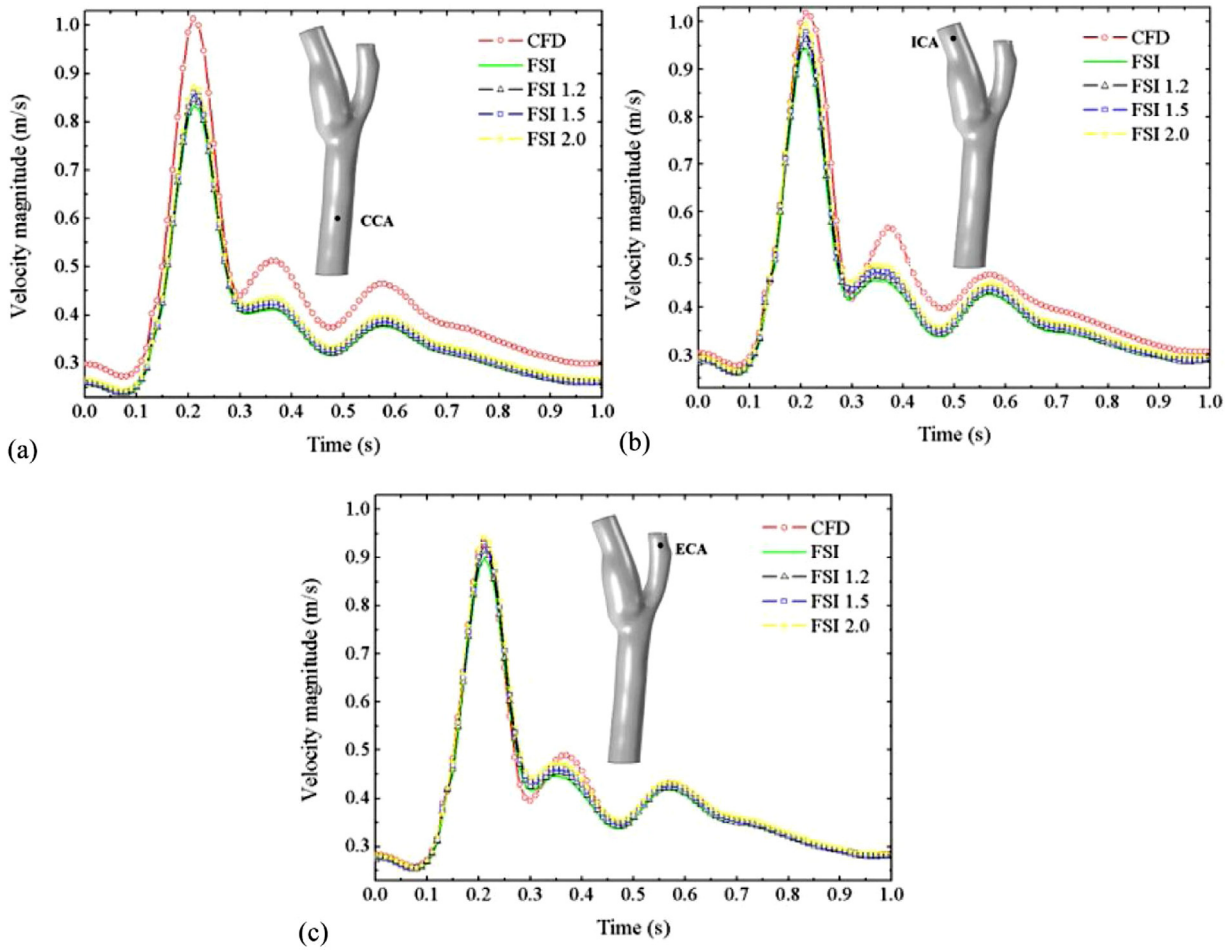

Fig. 8. Velocity magnitude taken from a point within the fluid domain. (a) CCA; (b) ICA; (c) ECA.

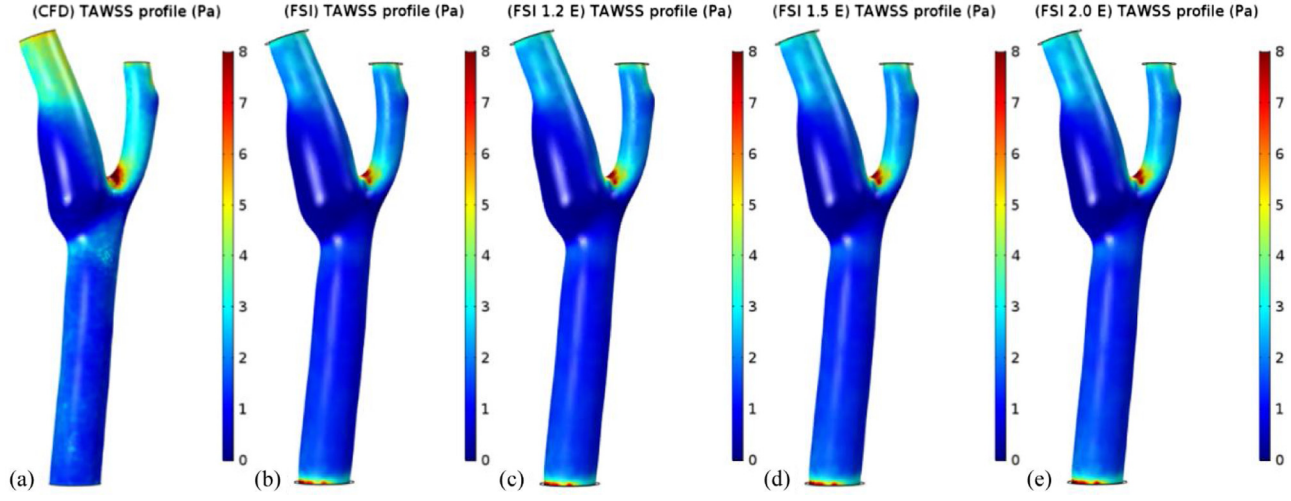

Fig. 9. Time-averaged wall shear stress profiles. (a) CFD; (b) FSI; (c) FSI 1.2 E; (d) FSI 1.5 E; (e) FSI 2.0 E.

velocity of FSI 2.0 E (in yellow) and FSI (in green) is found in the ICA point and is around 5%.

3.3. Wall shear stress

The Time-Averaged Wall Shear Stress profiles corresponding to the systolic peak for the performed simulations are represented in Fig. 9. Only the TAWSS values are shown in this paper, instead of the WSS at the systolic peak, which is when the parameter has maximum values since it is important to understand its behavior throughout the whole cardiac cycle and not just in an instant.

The results evidence high values of TAWSS at the apex of the bifurcation. The bifurcation forces blood to separate between the outlet arteries, and the blood is severely decelerated in this area, thus creating high-velocity gradients near the wall in this area. Previously, it has been shown that the flow suffered a deviation to the inner walls of the

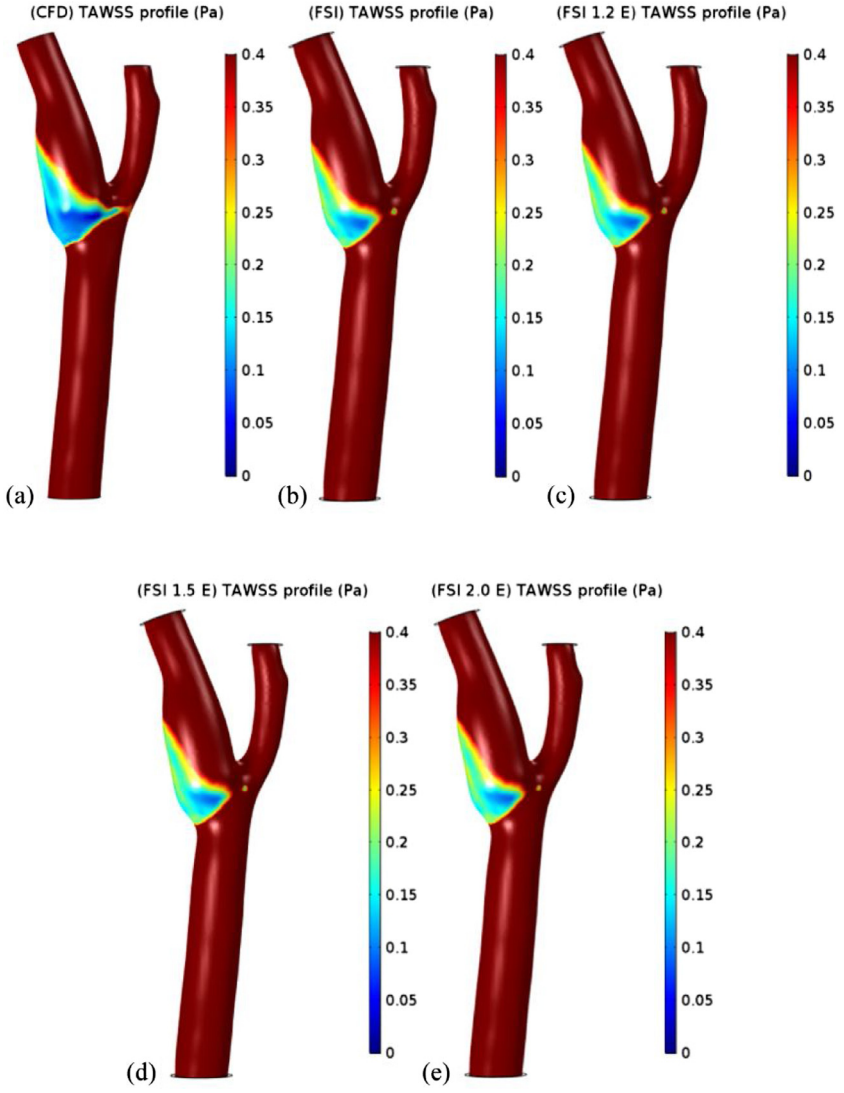

Fig. 10. Time-averaged wall shear stress profiles—reduced scale. (a) CFD; (b) FSI; (c) FSI 1.2 E; (d) FSI 1.5 E; (e) FSI 2.0 E.

ICA and ECA. These profiles reinforce that detail because the parameter has a higher value in those zones, contrary to what happens in the outer zones of the vessels, where the wall shear stress is lower. For the remainder of the geometry, it is verified that TAWSS is higher in the ICA and ECA than in the CCA. The results are in agreement with the work of [34].

Comparing the CFD and FSI studies, can be observed that the TAWSS is significantly higher in the CFD study, as expected, given the velocity profiles previously shown. Relatively to the FSI studies, the results are similar for all the values of the elastic modulus. Although differences were observed in the velocity profiles between the various FSI models, these were located primarily in the central zones of the vessels, and since this parameter only takes into account the behavior of the fluid at the wall, the similarity in the TAWSS is thereby justified.

As was previously mentioned, areas with TAWSS values lower than 0.4 Pa are prone to develop Atherosclerosis. In order to identify these zones, the scale of the profiles was adjusted to a maximum value of 0.4 Pa, as shown in Fig. 10.

Given the results of Fig. 10, it can be concluded that the carotid bulb is the area more favorable to the development of stenosis. In this zone, blood flow is reduced, hence the low TAWSS values, and exhibits several disturbances, such as fluid recirculation, which are conditions that prompt endothelial inflammation and, consequently, plaque accumulation. This observation was reported in several works [8,31,33,34]. It is noticed that the TAWSS profiles with reduced scale are similar for the FSI studies, while in the CFD study, these present a larger area that is subject to the referred values. The area of the outer wall surface was calculated, being approximately 1.34×10^{-3} m^2. It is emphasized that the surface area is variable between the studies of CFD and FSI given the expansion of the arterial wall. The percentage of the total area where the TAWSS is less than 0.4 Pa was also determined, with 13.24%, 10.15%, 12.85% 12.75% and 11.63% for CFD, FSI, FSI 1.2 E, FSI 1.5 E, and FSI 2.0 E, respectively, showing again that the CFD study overestimates the value of the TAWSS relatively to FSI.

3.4. Displacement

Fig. 11 represents the arterial wall displacement profiles of the FSI studies for the different values of the elastic modulus.

The results demonstrate that the instant of maximum displacement occurs at $t = 0.50$ s, which does not correspond to the moment of maximum flow rate, at the systolic peak. The maximum displacement occurs in a zone near the bifurcation apex, where the fluid pressure is higher. As the artery boundaries adjacent to the inlet and outlets were fixed, the displacement in these zones is null. Thereby, the pressure of the fluid is the main parameter that influences the displacement of the artery, since the moment of maximum displacement corresponds to the instant of maximum pressure imposed at the outlets, as a boundary condition.

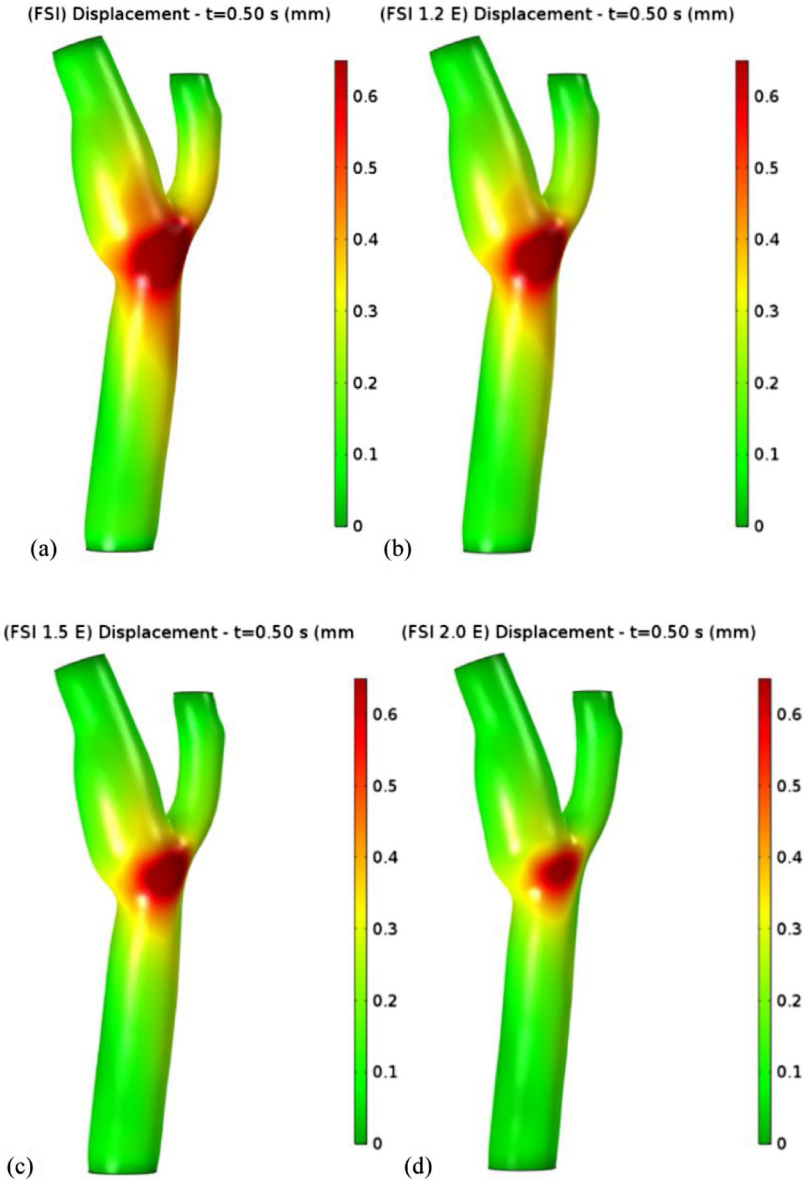

Fig. 11. Displacement profile at the arterial of the arterial wall ($t = 0.50$ s). (a) FSI; (b) FSI 1.2 E; (c) FSI 1.5 E; (d) FSI 2.0 E.

Additionally, it is observed that the displacement of the wall is higher for the lower values of the elastic modulus, as expected, which justifies the differences observed in the velocity profiles. For the FSI 2.0 study, as the wall displacement is lower, the increase of the lumen size is less significant, and as the dislocated blood volume is maintained, it is forced to move faster compared to what happens in the FSI study. As it is verified that the maximum displacement occurs precisely in near the bifurcation, it similarly affects the ICA and ECA lumen dimensions in the separation zone, thus justifying the resemblance of the flow separation graphs for all the studied cases, that were previously presented.

4. Conclusions

This paper presents a comparative study between a typical CFD problem, where only the fluid behavior is imputed, and a FSI problem, where the reciprocal influence of the fluid and solid is considered. Additionally, the progression of atherosclerosis is correlated to the hardening of the arteries, with the study of several FSI models of a patient-specific geometry of the carotid artery. The main conclusions drawn from this work are:

- Comparing the rigid (CFD) and elastic (FSI) walls studies, the velocity and WSS profiles are significantly overestimated on the rigid approach. It is therefore essential to consider the effect of the arterial wall on the blood flow.
- There is an increase in the magnitude of the velocity, with a maximum difference of about 5%, with the increment of the elastic modulus. This is related to the differences observed in the displacement profiles. Higher elastic modulus generates lower displacements of the arterial walls and elevated flow velocity.
- The lower values of TAWSS suggest that the carotid sinus is the more susceptible location to accumulate plaque and develop atherosclerosis.

Acknowledgments

This work was supported by FEDER funds through the COMPETE program with the reference project PTDC/SEM-TEC/3827/2014. Additionally, this work is supported by FCT with the reference projects UID/EEA/04436/2019, UID/CEC/00319/2019 and UID/EMS/04077/2019.

References

[1] Global Health Estimates 2016. Deaths by cause, age, sex, by country and region, 2000–2016. Geneva: World Health Organization; 2018.

[2] Xu S, Pelisek J, Jin ZG. Atherosclerosis is an epigenetic disease. Trends Endocrinol-Metabol 2018;29(11):739 –42. doi:10.1016/j.tem.2018.04.007.

[3] Oberoi S, Schoepf UJ, Meyer M, Henzler T, Rowe GW, Costello P, et al. Progression of arterial stiffness and coronary atherosclerosis: longitudinal evaluation by cardiac cT. Am JRoentgenol 2013;200(4):798–804. doi:10.2214/AJR.12.8653.

[4] Vlachopoulos C, Aznaouridis K, Stefanadis C. Prediction of cardiovascular events and all-cause mortality with arterial Stiffness: a systematic review and meta-analysis. J Am Coll Cardiol 2010;55(13):1318 –27. doi:10.1016/j.jacc.2009.10.061.

[5] Palombo C, Kozakova M. Arterial stiffness, atherosclerosis and cardiovascular risk: pathophysiologic mechanisms and emerging clinical indications. Vascul Pharmacol 2016;77:1–7. doi:10.1016/j.vph.2015.11.083.

[6] Abdolmaleki F, Gheibi Hayat SM, Bianconi V, Johnston TP, Sahebkar A. Atherosclerosis and immunity: a perspective. Trends Cardiovasc Med 2019;29(6):363–71. doi:10.1016/j.tcm.2018.09.017.

[7] Song P, Xia W, Zhu Y, Wang M, Chang X, Jin S, et al. Prevalence of carotid atherosclerosis and carotid plaque in Chinese adults: a systematic review and meta-regression analysis. Atherosclerosis 2018;276:67–73. doi:10.1016/j.atherosclerosis.2018.07.020.

[8] Gharahi H, Zambrano B, Zhu D, DeMarco K, Seungik B. Computational fluid dynamic simulation of human carotid artery bifurcation based on anatomy and volumetric blood flow rate measured with magnetic resonance imaging. Int J Adv Eng Sci Appl Math 2016;8(1):8. doi:10.1007/s12572-016-0161-6.

[9] Caro CG. Discovery of the role of wall shear in atherosclerosis. Arterioscler Thromb Vasc Biol 2009;29(2):158–61. doi:10.1161/ATVBAHA.108.166736.

[10] Zhang B, Gu J, Qian M, Niu L, Zhou H, Ghista D. Correlation between quantitative analysis of wall shear stress and intima-media thickness in atherosclerosis development in carotid arteries. Biomed Eng Online 2017;16(1):137. doi:10.1186/s12938-017-0425-9.

[11] Siasos G, Sara JD, Zaromytidou M, Park KH, Coskun AU, Lerman LO, et al. Local low shear stress and endothelial dysfunction in patients with nonobstructive coronary atherosclerosis. J Am Coll Cardiol 2018;71(19):2092 –102. doi:10.1016/j.jacc.2018.02.073.

[12] Chiastra C, Gallo D, Tasso P, Iannaccone F, Migliavacca F, Wentzel JJ, et al. Healthy and diseased coronary bifurcation geometries influence near-wall and intravascular flow: a computational exploration of the hemodynamic risk. J Biomech 2017;58:79–88. doi:10.1016/j.jbiomech.2017.04.016.

[13] Maier IL, Hofer S, Joseph AA, Merboldt KD, Tan Z, Schregel K, et al. Carotid artery flow as determined by real-time phase-contrast flow MRI and neurovascular ultrasound: a comparative study of healthy subjects. Eur J Radiol 2018;106:38–45. doi:10.1016/j.ejrad.2018.07.011.

[14] Brandt AH, Hansen KL, Ewertsen C, Holbek S, Olesen JB, Moshavegh R, et al. A comparison study of vector velocity, spectral doppler and magnetic resonance of blood flow in the common carotid artery. Ultrasound Med Biol 2018;44(8):1751 –61. doi:10.1016/j.ultrasmedbio.2018.05.002.

[15] He Y, Shiu Y-T, Pike DB, Roy-Chaudhury P, Cheung AK, Berceli SA. Comparison of hemodialysis arteriovenous fistula blood flow rates measured by Doppler ultrasound and phase-contrast magnetic resonance imaging. J Vasc Surg 2018;68(6):1848–57 e2. doi:10.1016/j.jvs.2018.02.043.

[16] Kim D-H, Shin S, Kim N, Choi T, Choi SH, Choi YS. Carotid ultrasound measurements for assessing fluid responsiveness in spontaneously breathing patients: corrected flow time and respirophasic variation in blood flow peak velocity. Br J Anaesth 2018;121(3):541 –9. doi:10.1016/j.bja.2017.12.047.

[17] Lynser D, Daniala C, Khan AY, Marbaniang E, Thangkhiew I. Effects of dynamic range variations on the Doppler flow velocities of common carotid arteries. Artery Res 2018;22:18–23. doi:10.1016/j.artres.2018.02.001.

[18] Gates PE, Gurung A, Mazzaro L, Aizawa K, Elyas S, Strain WD, et al. Measurement of wall shear stress exerted by flowing blood in the human carotid Artery: ultrasound Doppler velocimetry and echo particle image velocimetry. Ultrasound Med Biol 2018;44(7):1392 –401. doi:10.1016/j.ultrasmedbio.2018.02.013.

[19] Doutel E, Carneiro J, Campos JBLM, Miranda JM. Experimental and numerical methodology to analyze flows in a coronary bifurcation. Eur JMech B/Fluids 2018;67:341 –56. doi:10.1016/j.euromechflu.2017.09.009.

[20] Long Q, Xu X, Köhler U, B Robertson M, Marshall I, Hoskins P. Quantitative comparison of CFD predicted and MRI measured velocity fields in a carotid bifurcation phantom. Biorheology 2002;39:467 –74.

[21] Cibis M, Potters WV, Selwaness M, Gijsen FJ, Franco OH, Arias Lorza AM, et al. Relation between wall shear stress and carotid artery wall thickening MRI versus CFD. J Biomech 2016;49(5):735 –41. doi:10.1016/j.jbiomech.2016.02.004.

[22] Rispoli VC, Nielsen JF, Nayak KS, Carvalho JLA. Computational fluid dynamics simulations of blood flow regularized by 3D phase contrast MRI. Biomed Eng Online 2015;14(1). doi:10.1186/s12938-015-0104-7.

[23] Sousa LC, Castro CF, António CC. Blood flow simulation and applications. In: Natal Jorge RM, Tavares JMRS, Pinotti Barbosa M, Slade AP, editors. Technologies for medical sciences, 1. DordrechtNetherlands: Springer; 2012. p. 67–86. doi:10.1007/978-94-007-4068-6_4.

[24] Lee SH, Kang S, Hur N, Jeong S-K. A fluid-structure interaction analysis on hemodynamics in carotid artery based on patient-specific clinical data. J Mech Sci Technol 2012;26(12):3821 –31. doi:10.1007/s12206-012-1008-0.

[25] Nejad AA, Talebi Z, Cheraghali D, Shahbani-Zahiri A, Norouzi M. Pulsatile flow of non-Newtonian blood fluid inside stenosed arteries: investigating the effects of viscoelastic and elastic walls, arteriosclerosis, and polycythemia diseases. Comput Methods Programs Biomed 2018;154:109 –22. doi:10.1016/j.cmpb.2017.11.016.

[26] Khader A, Ayachit A, Pai R, Ahmed K, Rao V, Kamath G. Haemodynamics study in subject specific carotid bifurcation using FSI. Int J Mech Aerospace Ind Mechatron Manuf Eng 2014;8:1885–90.

[27] Sun Z. Aging, arterial stiffness and hypertension. Hypertension 2015;65:252 –6. doi:10.1161/HYPERTENSIONAHA.114.03617.

[28] Venkatesan J, Sankar DS, Hemalatha K, Yatim Y. Mathematical analysis of casson fluid model for blood rheology in stenosed narrow arteries. J Appl Math 2013;2013:1–11. doi:10.1155/2013/583809.

[29] Gidaspow D, Huang J. Kinetic theory based model for blood flow and its viscosity. Ann Biomed Eng 2009;37:1534 –45. doi:10.1007/s10439-009-9720-3.

[30] Shibeshi SS, Collins WE. The rheology of blood flow in a branched arterial system. Appl Rheol 2005;15:398–405. doi:10.1901/jaba.2005.15-398.

[31] Seo T. Hemodynamic characteristics in the human carotid artery model induced by blood-arterial wall interactions. Int J Biomed Biol Eng 2013;7:6.

[32] Souli M, Benson DJ, editors. Arbitrary lagrangian-eulerian and fluid-structure interaction: souli/arbitrary lagrangian-eulerian and fluid-structure interaction John Wiley & Sons, Inc., Hoboken, NJ USA; 2013. doi:10.1002/9781118557884.

[33] Sousa LC, Castro CF, António CC, Azevedo E. Fluid-Structure interaction modelling of blood flow in a non-stenosed common carotid artery bifurcation. 7th International Conference on Mechanics and Materials in Design Albufeira /Portugal; 2017.

[34] Moradicheghamahi J, Sadeghiseraji J, Jahangiri M. Numerical solution of the pulsatile, non-Newtonian and turbulent blood flow in a patient specific elastic carotid artery. Int J Mech Sci 2019;150:393–403. doi:10.1016/j.ijmecsci.2018.10.046.

[35] Saeid Khalafvand S, Han H-C. Stability of carotid artery under steady-state and pulsatile blood flow: a fluid–structure interaction study. J Biomech Eng 2015;137:061007. doi:10.1115/1.4030011.

[36] Moyle KR, Antiga L, Steinman DA. Inlet conditions for image-based CFD models of the carotid Bifurcation: is it reasonable to assume fully developed Flow? J Biomech Eng 2006;128:371. doi:10.1115/1.2187035.

[37] Arzani A, Shadden SC. Wall shear stress fixed points in cardiovascular fluid mechanics. J Biomech 2018;73:145 –52. doi:10.1016/j.jbiomech.2018.03.034.

[38] Malek AM. Hemodynamic shear stress and its role in atherosclerosis. JAMA 1999;282:2035. doi:10.1001/jama.282.21.2035.

[39] Kumar A, Hung OY, Piccinelli M, Eshtehardi P, Corban MT, Sternheim D, et al. Low coronary wall shear stress is associated with severe endothelial dysfunction in patients with nonobstructive coronary artery disease. JACC Cardiovasc Interven 2018;11:2072 –80. doi:10.1016/j.jcin.2018.07.004.

[40] Dolan JM, Kolega J, Meng H. High wall shear stress and spatial gradients in vascular Pathology: a review. Ann Biomed Eng 2013;41:1411 –27. doi:10.1007/s10439-012-0695-0.

[41] Marshall I, Papathanasopoulou P, Wartolowska K. Carotid flow rates and flow division at the bifurcation in healthy volunteers. Physiol Meas 2004;25:691 –7. doi:10.1088/0967-3334/25/3/009.